In Vivo Magnetic Resonance Image-Based 3D Computational Models to Quantify Right Ventricle Morphological and Mechanical Characteristics for Healthy and Patients with Tetralogy of Fallot

Heng Zuo,[1] †*Dalin Tang[1,2] Chun Yang,[1,3] Zheyang Wu,[1] Xueying Huang,[1,4]
Rahul H. Rathod,[5] Alexander Tang,[5] Kristen L. Billiar,[6,7] Tal Geva,[5]

[1] Mathematical Sciences Department, Worcester Polytechnic Institute, Worcester, MA 01609
[2] School of Biological Science & Medical Engineering, Southeast University, Nanjing, 210096, China
[3] China Information Tech. Designing & Consulting Institute Co., Ltd., Beijing, 100048, China
[4] School of Mathematical Sciences, Xiamen University, Xiamen, Fujian 361005, China
[5] Department of Cardiology, Boston Children's Hospital, Department of Pediatrics, Harvard Medical School, Boston, MA 02115 USA
[6] Department of Biomedical Engineering, Worcester Polytechnic Institute, MA 01609, USA
[7] Department of Surgery, University of Massachusetts Medical School, Worcester, MA 01655

*† Presenting and corresponding author: Dalin Tang, Southeast University, Nanjing China; Mathematical Sciences Department, Worcester Polytechnic Institute, Worcester, MA 01609, email: dtang@wpi.edu , fax: 508 831-5824

Abstract

Patients with repaired tetralogy of Fallot (TOF) account for the majority of cases with late onset right ventricle (RV) failure. It is a challenge to differentiate patient with better outcome after pulmonary valve replacement (PVR) from patients with worse outcome. Comparing TOF patients with healthy people may provide information to address this challenge.

Cardiac magnetic resonance (CMR) data were obtained from 16 TOF patients (8 male, median age, 42.75) and 6 healthy group (HG) volunteers (1 male, median age, 20.1). The patients with positive ejection fraction (EF) changes after PVR form the better-outcome patient group (BPG, n=5). The patients with negative EF changes is called the worse-outcome patient group (WPG, n=11). CMR-based patient-specific computational RV/LV models were constructed to obtain RV wall thickness (WT), volumes, curvature, and mechanical stress and strain for analysis.

At begin-of-ejection, BPG stress was very close to HG stress (54.7±38.4 kPa vs. 51.2±55.7 kPa, p=0.6889) while WPG stress was much higher than HG stress (94.3±89.2 kPa vs. 51.2±55.7 kPa, p=0.0418). BPG RV volume was 43.3% higher than HG RV volume while WPG RV volume was 108.1% higher than that from HG. BPG longitudinal curvature (L-cur) was 65.1% higher than HG L-cur, while WPG L-cur was 26.7% higher than HG L-cur. Circumferential curvature, RV strain and wall thickness did not provide much useful information.

BPG stress was shown to be close to HG stress and stress may be used as an indicator to differentiate BPG patients from WPG patients, with further validations.

Keywords: ventricle modeling, cardiac mechanics, magnetic resonance imaging, normal ventricle, right ventricle, tetralogy of Fallot.

1. Introduction

With the recent development of computational modelling and medical imaging technology, computer modeling and computer-aided procedures become more widely used in cardiac function analysis and patient-specific surgical design, replacing traditional empirical and often risky experimentation to examine the efficiency and suitability of various reconstructive cardiac procedures. Recent reviews are given in [1-4]. In this paper, patient-specific computational models based on cardiac magnetic resonance (CMR) imaging were used to quantify right ventricle morphological and mechanical characteristics for healthy and patients with tetralogy of Fallot (TOF). These information would form basis for further cardiac research and for potential clinical applications treat TOF patients.

Tetralogy of Fallot (TOF) is a congenital heart defect which involves four anatomical abnormalities of the heart: pulmonary infundibular stenosis, overriding aorta, ventricular septal defect and right ventricular hypertrophy. With the introduction of TOF repair surgery, survival of TOF patients has increased a lot starting from the 80s. Recently, the relevant reports show that long-term survival rate for repaired TOF patients decreased significantly after the first two decades of the initial repair [5]. In the third and fourth decade after initial surgery, lots of patients with repaired TOF present severe right ventricle (RV) dilation and dysfunction which is caused by the residual anatomic defects left by initial TOF repair. The defects, including pulmonary regurgitation and scarred myocardium from the ventriculotomy, lead to the late onset RV failure. Pulmonary valve replacement (PVR), which mainly addresses chronic pulmonary regurgitation, is one traditional surgical approach for repaired TOF patients with failing RV. Although the current PVR surgical approaches address pulmonary regurgitation issue, many patients do not experience an improvement in RV function and some show a decline after PVR [6-12].

In our previous publications, 3D computational RV/LV models were constructed based on cardiac magnetic resonance (CMR) imaging data for TOF patients to investigate and optimize PVR surgery. In [13,14], computational ventricular models were used in the comparison between regular PVR surgeries and PVR surgeries with RV remodeling, and PVR surgeries with RV remodeling were found to result in reduced stress/strain conditions in the patch area which may lead to improved recovery of RV function. In [15], computational ventricular models with different patch materials were constructed and solved to evaluate the effect of patch materials on RV function. In [16], computational ventricular models with contracting band were built to investigate the impact of band material stiffness variations, band length and active contraction. These results indicated that computational models were powerful in the investigation of PVR surgeries.

In this study, CMR-based computational RV/LV models were constructed for 6 healthy people and 16 TOF patients. The purposes of this study are: a) obtain RV morphological and mechanical parameters (circumferential and longitudinal curvature, RV stress and strain) for healthy people which are lacking in the current literatures; b) find the differences in morphological and mechanical stress/strain characteristics between TOF patients and healthy people and see if this will help to differentiate better outcome TOF patients from worse outcome TOF patients.

2. Data acquisition, models and methods

2.1 Data acquisition

This study was approved by the Boston Children's Hospital Committee on Clinical Investigation. CMR data were obtained from 22 people (9 male, 13 female; median age, 36.6 years; 16 with TOF, 6 healthy) previously enrolled in our RV surgical remodeling trial [17]. For the 16 TOF patients, CMR data before and 6 months after PVR were available for model construction and analysis. Based on their RV ejection fraction (EF) changes, the patients were categorized into two groups, the Better-Outcome Patient Group (BPG, n=5) which had positive RV EF changes (RV EF change: 3.94 ± 2.20) and Worse-Outcome Patient Group (WPG, n=11) which had negative RV EF changes (RV EF change: -8.88 ± 5.30, p-value: 0.00015). Demographic information, RV volumes, pressure conditions, and RV EF for the participants are summarized in Table 1.

Table 1. Demographic and CMR data for healthy volunteers and TOF patients.

Patient	Sex	Age (y)	Begin-Filling Pressure	Begin-Ejection Pressure	RV EDV (cm^3)	RV ESV (cm^3)	RV EF (%)	ΔEF (%)
Healthy Group								
H1	F	46.7	3.6	22	128.4	46.9	63	-
H2	M	23.6	5	27.9	226.6	105.4	53	-
H3	M	20.8	4.5	24	231.7	107.0	54	-
H4	M	19.4	3.9	23.8	213.5	94.2	56	-
H5	M	17.7	4.2	24.3	233.7	105.5	55	-
H6	M	6.7	4.3	24.8	67.6	28.2	58	-
Mean ± SD		22.5 ±13.2	4.25 ±0.48	24.5 ±1.93	183.6 ±69.4	81.2 ±34.6	56.5 ±3.62	-
Better-Outcome Patient Group								
P1	M	22.5	21.6	31.4	406.9	254.5	37.5	1.4
P2	F	42.0	10	45	323.3	177.8	45.0	4.0
P3	F	14.3	3	29	204.0	104.3	48.8	5.6
P4	F	15.3	2	15	193.7	105.1	45.7	6.6
P5	M	17.0	3	27	188.3	108.3	42.5	2.0
Mean ± SD		22.2 ±11.5	7.92 ±8.29	29.5 ±10.7	263.2 ±97.7	150.0 ±66.2	43.9 ±4.22	3.92 ±2.24
Worse-Outcome Patient Group								
P6	F	38.5	6	28	328.8	196.0	40.4	-3.4
P7	M	47.7	2	31	408.8	254.8	37.7	-2.6
P8	M	50.0	3	33	364.6	239.5	34.3	-2.9
P9	F	56.9	5	41	385.1	184.6	52.1	-18.0
P10	M	11.6	10	36	204.2	121.3	40.6	-8.4
P11	M	43.5	17	65	665.1	464.0	30.2	-15.2
P12	M	54.1	4	63	334.8	170.8	49.0	-7.0
P13	F	49.5	12	52	277.2	151.3	45.4	-5.0
P14	M	17.8	2	30	365.0	178.0	51.2	-9.5
P15	F	44.6	11	50	299.0	186.0	37.8	-12.3
P16	F	45.3	9	49	571.1	371.3	35.0	-13.4
Mean ± SD		41.8 ±14.4	7.36 ±4.82	43.5 ±13.2	382.2 ±131	228.9 ±102	41.2 ±7.27	-8.88 ±5.29

Abbreviations: F: Female; M: male; EDV: end-diastolic volume; ESV: end-systolic volume; EF: ejection fraction.

CMR acquisition procedures have been previously described [13-16,18] and were omitted here. Each CMR data set consists of 30 time steps per cardiac cycle, and each time step data has 9-14 equidistant slices covering ventricles in ventricular short axis from base to apex. Three-dimensional RV/LV geometry and computational meshes were constructed following the procedures described in [13-15]. Figure 1 shows one set of CMR images from a TOF patient before the PVR surgery with segmented contours and re-constructed 3D RV/LV geometries. Our two-layer model construction and fiber orientation information were also provided [2,19].

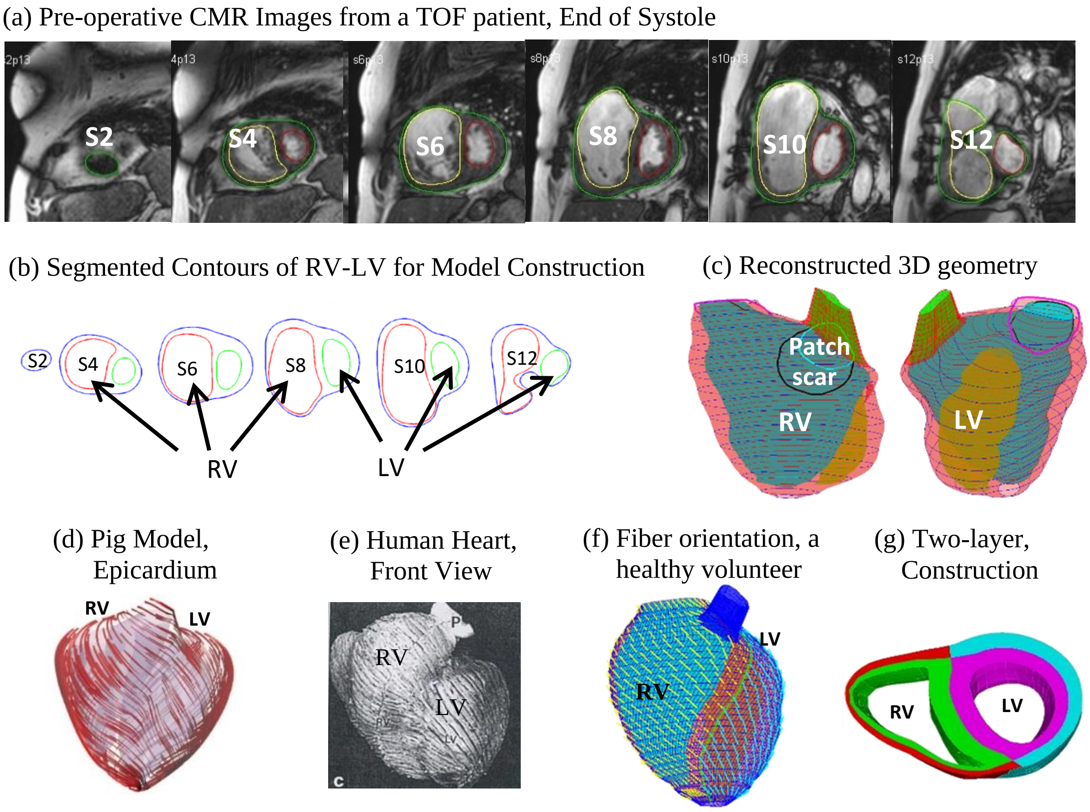

Figure 1. Illustration of model construction procedure using selected CMR image slices from a TOF patient. (a) Pre-operative CMR images of a TOF patient; (b) segmented contours; (c) reconstructed 3D geometry; (d-e) fiber orientation from a pig model [16] and a human heart [13]; (f) fiber orientation from one RV/LV model of a healthy volunteer; (g) two-layer construction.

2.2 The active anisotropic RV/LV models

The ventricular material was assumed to be hyperelastic, anisotropic, nearly-incompressible and homogeneous. Right Ventricular Outflow Tract (RVOT) material, patch and scar were assumed to be hyper-elastic, isotropic, nearly-incompressible and homogeneous. The governing equations for the structure models are:

$$\rho \frac{\partial^2 u_i}{\partial t^2} = \frac{\partial \sigma_{ij}}{\partial x_j}, \; i = 1, 2, 3 \tag{1}$$

$$\varepsilon_{ij} = \frac{1}{2}\left(\frac{\partial u_j}{\partial a_i} + \frac{\partial u_i}{\partial a_j} + \sum_l \frac{\partial u_l}{\partial a_i}\frac{\partial u_l}{\partial a_j}\right), \; i, j = 1, 2, 3 \tag{2}$$

Here $\boldsymbol{\sigma}$ is the stress tensor, $\boldsymbol{\varepsilon}$ is Green's strain tensor, $\boldsymbol{u}$ is the displacement, and ρ is material density.

The normal stress on the outer RV/LV surface was assumed to be zero. On the inner RV/LV surfaces, the normal stress was assumed to be equal to the imposed RV/LV pressure conditions:

$$P|_{RV} = P_{RV}(t)\ ,\ P|_{LV} = P_{LV}(t) \tag{3}$$

The nonlinear Mooney-Rivlin model was used to describe the nonlinear anisotropic and isotropic material properties. The strain energy function for the isotropic modified Mooney-Rivlin model (used for patch, scar tissue and RVOT material) was given by Tang et al. [16-18]:

$$W = c_1(I_1 - 3) + c_2(I_2 - 3) + D_1[\exp\big(D_2(I_1 - 3)\big) - 1] \tag{4}$$

$$I_1 = \sum C_{ii}\ ,\ I_2 = \frac{1}{2}[I_i^2 - C_{ij}C_{ij}] \tag{5}$$

where I_1 and I_2 are the first and second strain invariants, $C = [C_{ij}] = X^T X$ is the right Cauchy–Green deformation tensor, $\boldsymbol{X}$=$[X_{ij}] = [\partial x_i/\partial a_j]$ ((x_i) is current position, (a_i) is original position), and c_i and D_i are material parameters chosen to match experimental measurements [13,20].

The strain energy function for the anisotropic modified Mooney-Rivlin model was used for the ventricle tissue [14, 15]:

$$W = c_1(I_1 - 3) + c_2(I_2 - 3) + D_1\big[\exp\big(D_2(I_1 - 3)\big) - 1\big] + K_1/(K_2)\exp[K_2(I_4 - 1)^2 - 1] \tag{6}$$

where $I_4 = C_{ij}(\mathbf{n}_\mathrm{f})_i(\mathbf{n}_\mathrm{f})_j$, C_{ij} is the Cauchy-Green deformation tensor, $\mathbf{n}_\mathrm{f}$ is the fiber direction, K_1 and K_2 are material constants. The anisotropic (transversely isotropic) strain-energy function with respect to the local fiber direction was given below [1].

$$W = \frac{C}{2}(e^Q - 1) \tag{7}$$

$$Q = b_1 E_{ff}^2 + b_2(E_{cc}^2 + E_{rr}^2 + E_{cr}^2 + E_{rc}^2) + b_3(E_{fc}^2 + E_{cf}^2 + E_{fr}^2 + E_{rf}^2) \tag{8}$$

where E_{ff} is fiber strain, E_{cc} is cross-fiber in-plane strain, E_{rr} is radial strain, and E_{cr}, E_{fr} *and* E_{fc} are the shear components in their respective coordinate planes, C, b_1, b_2, and b_3 are parameters to be chosen to fit experimental data. It should be noted that Equations (7)-(8) were used because it is desirable to use local coordinate system to identify material parameters which are independent of fiber directions.

Biaxial mechanical testing of human myocardium was performed in Billiar's lab and results were reported in our previous paper (see Figure 2) [21]. Active contraction and relaxation were modeled by material stiffening and softening. In our material model, parameter values c_1, D_1 and C in equations (6) and (7) were adjusted at every CMR time step to match CMR-measured RV volume data for each patient. Patient-specific stress-stretch curves derived from the modified Mooney-Rivlin models for one healthy volunteer at begin of filling and begin of ejection were given in Figure 2 (d). Fiber orientation was set the same way as in our previous papers (see Figure 1) [2,19,21].

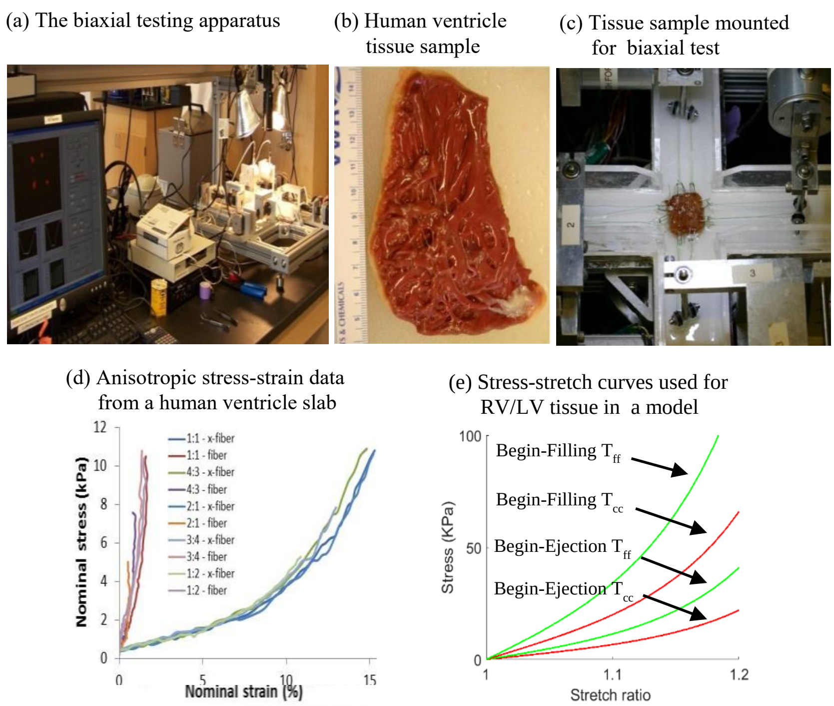

Figure 2. Biaxial mechanical testing and Stress-Stretch curves in the RV/LV model for a healthy volunteer with parameter values chosen to fit CMR data. (a) The biaxial testing apparatus in Dr. Billiar's lab; (b) a human right ventricle tissue sample; (c) tissue sample mounted for biaxial test; (d) anisotropic data from biaxial testing using human RV tissue sample; (e) stress-stretch curves from a healthy volunteer used in our RV/LV model. Model parameter values in Eq. (7)-(8): Begin-Filling (BF): C=27.06 kPa, b_1=8.7875; b_2=1.7005; b_3=0.7743; Begin-Ejection (BE): C=9.02 kPa, b_1=8.7875; b_2=1.7005; b_3=0.7743. T_{ff}: Stress in the fiber direction; T_{cc}: Stress in fiber circumferential direction.

2.3 Geometry-fitting Mesh Generation

In our patient-specific ventricular models, ventricles have complex irregular geometries which are challenging for mesh generation. A geometry-fitting mesh generation technique was developed to generate mesh for our models. Figure 1(g) gives an illustration of RV/LV geometry between two slices. In each slice, points were firstly defined based on the results of MRI segmentation. Then, lines were defined to divide the slice into geometry-fitting areas (called "surfaces" in ADINA). The neighboring slices were stacked to form volumes. Using this technique, the 3D RV/LV domain was divided into many small "volumes" to curve-fit the irregular ventricular geometry with patch and scar as inclusions. Finally, meshes were generated in each small volume. 3D surfaces, volumes and computational mesh were made under ADINA computing environment. Figure 3 shows the mesh generation technique by using two neighboring slices. For the H1 model constructed in this paper, the finite element ADINA structure model had 20688 meshes. Mesh analysis was performed by decreasing mesh size by 10% (in each dimension) until solution differences were less than 2%. The mesh was then chosen for our simulations.

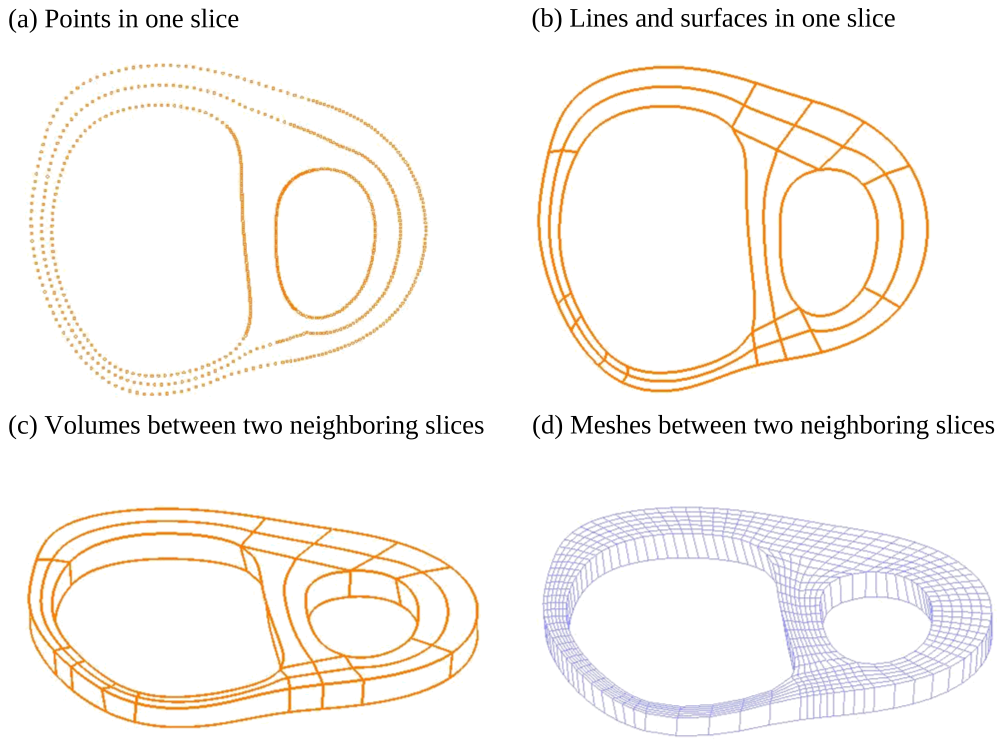

Figure 3. Geometry-fitting mesh generation processing. (a) Points defined in one slice, (b) Lines defined in one slice and lines divided the slice into geometry-fitting surfaces, (c) Volumes defined between two neighboring slices, (d) Generated meshes between two neighboring slices.

2.4 Pre-shrink process

Numerical simulation needs to start from an initial condition where the initial ventricular geometry, pressure and stress/strain conditions of a working heart were provided. Since stress conditions are too hard to be measured in vivo, our numerical simulations started from zero-load ventricular geometries with zero pressure and zero stress/strain distributions. Under the in vivo condition, the ventricles were pressurized and the zero-load ventricular geometries were not known. In our model construction process, a pre-shrink process was applied to the in vivo begin-filling ventricular geometries to generate the starting shape (zero-load ventricular geometries) for the computational simulation. The initial shrinkage for the inner ventricular surface was 2-3% and begin-filling pressure was applied so that the ventricles would regain its in vivo morphology. The ventricular out surface shrinkage was determined by conservation of mass so that the total ventricular wall mass was conserved. Without this pre-shrink process, the actual computing domain would be greater than the actual ventricle due to the initial expansion when pressure was applied.

2.5 Solution methods and morphological and stress/strain data for analysis

The RV/LV computational models (n=22) were constructed and solved by ADINA (ADINA R&D, Watertown, Mass) using finite elements and the New-Raphson iteration method. CMR-measured RV volume and pressure data were used to adjust model parameters so that model-predicted RV volume matched CMR-measure data.

Each ventricle model had 9-14 CMR slices. Every slice was divided into 4 quarters, each with equal inner wall circumferential length. Ventricular wall thickness (WT), circumferential curvature (C-cur), longitudinal curvature (L-cur), maximal principle stress (Stress-P_1) and maximal principle strain (Strain- P_1) were calculated at all nodal points (100 points per slice, 25 points per quarter). Their average values over the 25 points in each quarter provided the "quarter" values of these parameters. Those values were collected for analysis. The formulas used for calculation of circumferential curvature (κ_c) at each point was

$$\kappa_c = \frac{x'y''-x''y'}{(x'^2+y'^2)^{3/2}} \tag{9}$$

The formulas used for calculation of longitudinal curvature (κ) at each point was

$$\kappa = \frac{\sqrt{(z''(t)y'(t)-y''(t)z'(t))^2+(x''(t)z'(t)-z''(t)x'(t))^2+(y''(t)x'(t)-x''(t)y'(t))^2}}{(x'^2(t)+y'^2(t)+z'^2(t))^{3/2}} \tag{10}$$

Details can be found from [21].

2.6 Statistical analysis

Continuous variables (RV volumes, WT, C-cur, L-cur, Stress-P_1 and Strain-P_1 values) were summarized as mean standard deviation or median (range). Unpaired Student *t* test was used to compare mean RV volumes between different groups. Due to the small size of data, the quarter mean values were used in the analysis of RV wall thickness, curvatures, Stress-P_1 and Strain-P_1. Similar to what we did in [21], the Linear Mixed-Effect Model (LMM) was used to take care of data dependence structure and compare quarter mean values of RV WT, C-cur and L-cur, Stress-P_1 and Strain-P_1 between different outcome groups.

3. Results

3.1 Results from Healthy Group

Table 2 summarized the average values of the geometrical and mechanical parameters from all the 6 computational models of healthy volunteers at begin of ejection. At the beginning of ejection, mean WT of healthy group (HG) was 0.51 cm. Average C-cur and L-cur from HG were 0.81 1/cm and 0.85 1/cm respectively. Mean RV volume of HG was 183.6 cm^3. Average HG Stress-P_1 and Strain-P_1 were 51.3 kPa and 0.51. These values from the healthy group would be used as the baseline in the following investigation.

Table 2. Summary of mean geometric and stress/strain parameter values at begin of ejection.

	WT (cm)	C-cur (1/cm)	L-cur (1/cm)	RV EDV (cm^3)	Stress-P_1 (kPa)	Strain-P_1
HG						
H1	0.35	1.15	0.87	125.2	70.2	0.63
H2	0.68	0.68	0.56	227.1	51.6	0.58
H3	0.64	0.77	0.68	226.7	36.3	0.40
H4	0.51	0.62	0.61	213.1	56.0	0.39
H5	0.57	0.57	1.27	232.6	45.9	0.57
H6	0.31	0.90	1.11	66.37	48.0	0.51
Mean ± SD	0.51 ±0.15	0.81 ±0.19	0.85 ±0.29	183.6 ±69.4	51.3 ±11.4	0.51 ±0.10
BPG						
P1	0.39	0.47	1.24	406.9	56.9	0.29
P2	0.47	0.43	0.96	323.3	82.4	0.44
P3	0.48	0.50	1.20	204.0	61.9	0.48
P4	0.42	0.53	1.84	193.7	33.5	0.46
P5	0.51	0.53	1.85	188.3	42.0	0.40
Mean ± SD	0.45 ±0.05	0.49 ±0.04	1.42 ±0.40	263.2 ±97.7	55.3 ±18.9	0.41 ±0.08
WPG						
P6	0.34	0.39	0.77	328.8	65.3	0.43
P7	0.65	0.37	1.01	408.8	41.0	0.33
P8	0.49	0.54	1.54	364.6	64.1	0.36
P9	0.48	0.42	0.91	385.1	172.1	0.66
P10	0.41	1.34	1.32	204.2	82.9	0.49
P11	0.80	0.36	0.59	665.1	82.4	0.23
P12	0.71	0.44	0.72	334.8	83.1	0.42
P13	0.45	0.46	0.97	277.2	191.7	0.66
P14	0.43	0.65	1.60	365.0	65.4	0.44
P15	0.46	0.44	1.23	299.0	154.3	0.51
P16	0.59	0.33	1.25	571.1	76.2	0.34
Mean ± SD	0.53 ±0.14	0.52 ±0.29	1.08 ±0.33	382.2 ±131.1	98.0 ±50.1	0.44 ±0.13

Abbreviations: WT: wall thickness; C-cur: circumferential curvature; L-cur: longitudinal curvature; RV: right ventricle.

3.2 Comparison of geometrical parameters: TOF patients have noticeable differences in RV volume, L-cur and C-cur from healthy group

Table 3 summarized and compared the average values of geometrical parameters (RV volume, wall thickness, L-cur and C-cur) between healthy group (HG) and patient group (PG = BPG + WPG). Bar plots of the average values are given in Figure 4 showing group differences. RV volume was the parameter with the most noticeable difference between HG and PG. At the beginning of ejection, average PG RV volume was 87.9% higher than that from HG (344.9±131.3 cm^3 vs. 183.6±69.4 cm^3, p=0.0102). At the beginning of filling, average RV volume of PG was 151.5% higher than that from HG (204.2±97.9 cm^3 vs. 81.2±34.6 cm^3, p=0.0076). The high percentage difference at begin-filling was due to the fact that RV of PG contracted much less that HG.

C-cur and L-cur also showed large differences between HG and PG. At begin of ejection, mean PG C-cur was 35.8% lower than mean HG C-cur (0.52 ± 1.21 1/cm vs. 0.81 ± 1.05 1/cm, p=0.0237), and mean PG L-cur was 38.4% higher than mean HG L-cur (1.19 ± 1.21 1/cm vs. 0.86 ± 0.71 1/cm, p=0.0756). At begin of filling, average C-cur of PG was 22.9% lower than that from HG (0.64 ± 1.23 1/cm vs. 0.83 ± 0.51 1/cm, p=0.1519), and average L-cur of PG was 23.2% higher than that from HG (1.22 ± 1.22 1/cm vs. 0.99 ± 0.66 1/cm, p=0.2585).

It is worth noting that the ratio of L-cur over C-cur for PG at begin-ejection is 2.29, compared to 1.06 for HG. At begin of filling, the ratio of L-cur over C-cur for PG is 1.90, compared to 1.19 for HG. So PG average RV longitudinal curvature is 100% greater than PG average circumferential curvature, while L-curvature and C-curvature for HG were about equal.

RV WT did not show much differences between HG and PG. That is clear from both Fig. 4 and Table 3.

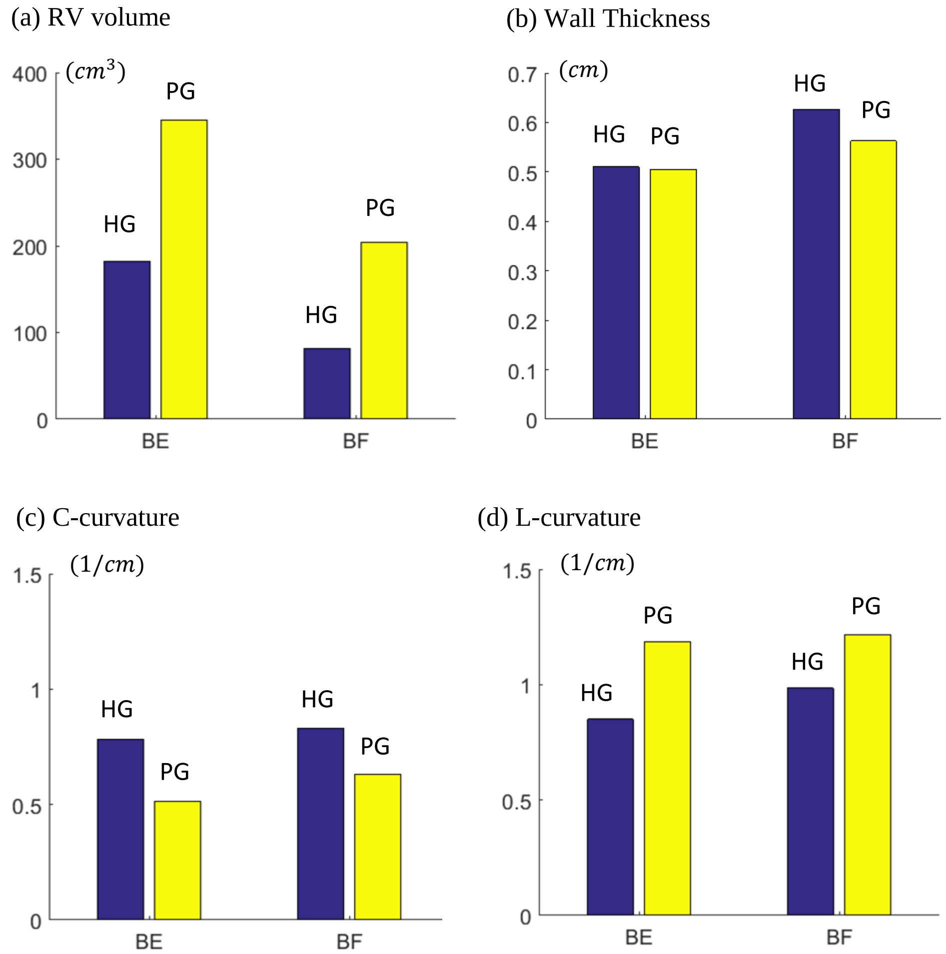

Figure 4. Bar plots comparing average RV volume, WT, C-cur, L-cur values from Healthy Group (HG) and Patient Group (HG) at Begin-Ejection (BE) and Begin-Filling (BF). Blue: HG; Yellow: PG.

Table 3. Comparison of RV volumes, geometric parameters, and stress/strain values between healthy group (HG) and patient group (PG=BPG+WPG) at begin of ejection and begin of filling.

	Begin of Ejection			**Begin of Filling**		
	PG	HG	P value	PG	HG	P value
RV volume (cm^3)	344.9±131.3	183.6±69.4	0.0102	204.2±97.9	81.2±34.6	0.0076
WT (cm)	0.51±0.24	0.51±0.30	0.9315	0.57±0.27	0.64±0.32	0.3616
C-cur (1/cm)	0.52±1.21	0.81±1.05	0.0237	0.64±1.23	0.83±0.51	0.1519
L-cur (1/cm)	1.19±1.21	0.86±0.71	0.0756	1.22±1.22	0.99±0.66	0.2585
Stress-P_1 (kPa)	82.2±79.4	51.2±55.7	0.1031	7.31±8.49	3.00±2.30	0.0831
Strain-P_1	0.43±0.19	0.51±0.17	0.1486	0.06±0.07	0.07±0.06	0.5376

Data is based on quarter mean values. Values are expressed as mean±standard deviation. Abbreviations as in Table 2.

3.3 Comparison of mechanical parameters: Stress-P_1 shows a large difference between TOF patient group and healthy group

Figure 5 gave stress and strain plots of one healthy volunteer and one TOF patient at Begin-Ejection and Begin-Filling respectively. Without patch and scar, Stress-P_1 and Strain-P_1 distributions of the healthy volunteer were more uniform than that from the TOF patient model near the patch area. Table 3 also summarized and compared RV maximum principal stress and strain (denoted by Stress-P_1 and Strain-P_1) between HG and PG. Figure 6 gave the bar plots of average stress and strain values, showing clear comparisons between healthy group and patient group.

At the beginning of ejection, average Stress-P_1 of PG was 60.5% higher than that from HG (82.2±79.4 kPa vs. 51.2±55.7 kPa, p=0.1031). At the beginning of filling, mean Stress-P_1 of PG was 143.7% higher than that from HG (7.31±8.49 kPa vs. 3.00±2.30 kPa, p=0.0831). The high percentage should be discounted because the overall stress values were small. At begin of ejection, average Strain-P_1 from HG was 18% higher than that from PG. Noticing that average Strain-P1 values from both HG and PG at begin-filling were about the same, higher strain from HG means that healthy ventricles had better contractibility, consistent with our expectations.

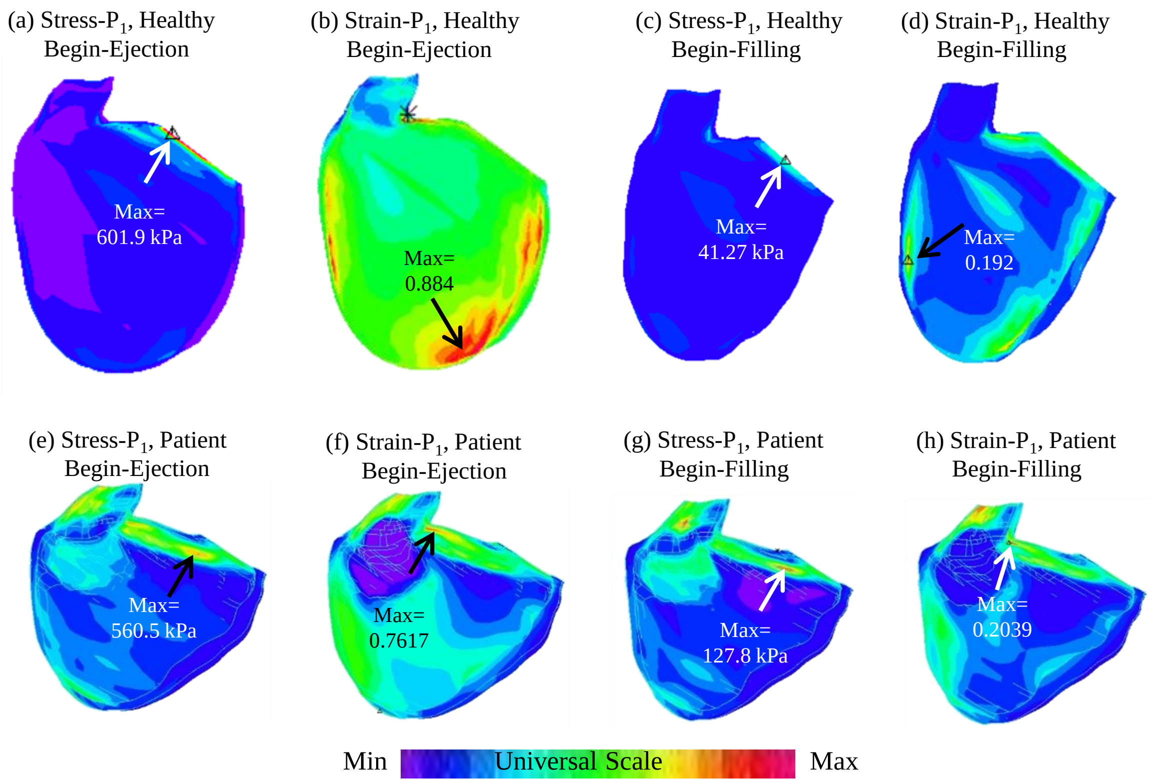

Figure 5. Stress and strain plots from one healthy volunteer (a)-(d) and one TOF patient (e)-(h) showing stress/strain distribution patterns.

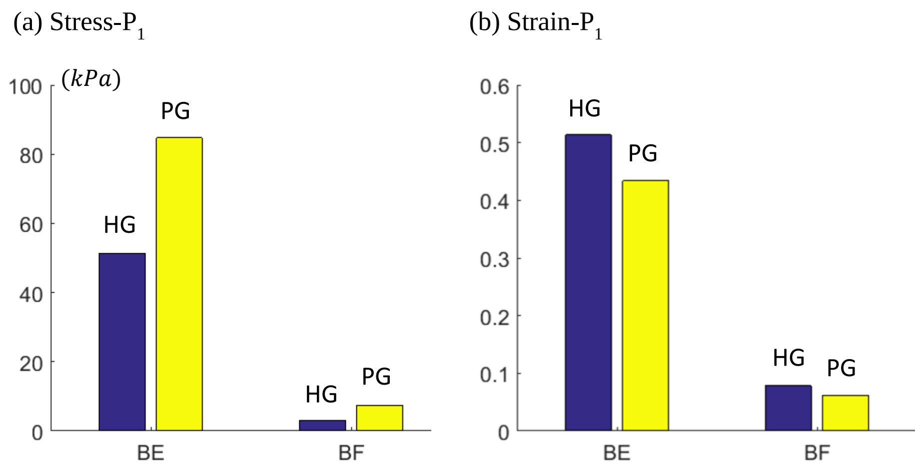

Figure 6. Bar plots comparing average Stress-P_1 and Strain-P_1 values from Healthy Group (HG) and Patient Group (HG) at Begin-Ejection (BE) and Begin-Filling (BF). Blue: HG; Yellow: PG.

3.4 HG may help differentiate BPG from WPG

Table 4 summarized and compared geometrical and mechanical parameter values of BPG and WPG to HG. Figure 7 gave the bar plots of average Stress-P_1, Strain-P_1, RV volume, C-cur, L-cur and WT at begin-ejection, showing the differences among the three groups. Table 4 and Figure 7 showed that differences in wall thickness, C-cur and Strain-P1 between BPG and WPG may not be very useful in differentiating BPG patients from WPG patients.

Stress-P_1 from BPG was found to be closer to that from HG, compared to Stress-P_1 of WPG. At the beginning of ejection, mean Stress-P_1 of BPG was only 6.8% higher than that from HG (54.7±38.4 kPa vs. 51.2±55.7 kPa, p=0.6889), and the difference was not significant; while average Stress-P_1 of WPG was 84.1% higher than that of HG (94.3±89.2 kPa vs. 51.2±55.7 kPa, p=0.0418), and the difference was significant. At the beginning of filling, average Stress-P_1 of BPG was 25% higher than that from HG (3.76±4.17 kPa vs. 3.00±2.30 kPa, p=0.5968), while average Stress-P_1 of WPG was 195.7% higher than that of HG (8.87±9.39 kPa vs. 3.00±2.30 kPa, p=0.0290). The results suggested that comparing patient's RV stress values with healthy RV stress values may help identify patients with possible better outcome.

Similarly, BPG RV volumes at Begin-Ejection were closer to HG RV volumes (263 cm^3 vs. 184 cm^3, 43% higher) compared to WPG volumes (382 cm^3 vs. 184 cm^3, 107% higher). BPG L-curvature was much greater than HG L-curvature at Begin-Ejection (1.42 vs. 0.86 1/cm, 65% higher) than WPG L-cur over HG (1.09 vs. 0.86 1/cm, 27% higher). Based on these results, RV volume and L-cur could be useful in identifying better-outcome patients.

Table 4. Comparison of geometric and stress/strain mean values between healthy group (HG) and patient groups (better-outcome patient group (BPG), worse-outcome patient group (WPG) at begin of ejection and begin of filling.

	Begin of Ejection (maximal volume and pressure)			**Begin of Filling (minimal volume and pressure)**		
	BPG	HG	P value	BPG	HG	P value
RV volume (cm^3)	263.2±97.7	183.6±69.4	0.1482	150.0±66.2	81.2±34.6	0.0534
WT (cm)	0.45±0.20	0.52±0.30	0.4441	0.50±0.21	0.64±0.32	0.1099
C-cur (1/cm)	0.49±0.26	0.81±1.05	0.0094	0.63±0.34	0.83±0.51	0.0082
L-cur (1/cm)	1.42±1.40	0.86±0.71	0.0263	1.58±1.56	0.99±0.66	0.0420
Stress-P_1 (kPa)	54.7±38.4	51.2±55.7	0.6889	3.76±4.17	3.00±2.30	0.5968
Strain-P_1	0.41±0.18	0.51±0.17	0.1042	0.03±0.02	0.07±0.06	0.1047
	WPG	HG	P value	WPG	HG	P value
RV volume (cm^3)	382.1±131.1	183.6±69.4	0.0038	228±102.4	81.2±34.6	0.0041
WT (cm)	0.53±0.26	0.52±0.30	0.8150	0.60±0.29	0.64±0.32	0.6508
C-cur (1/cm)	0.54±1.45	0.81±1.05	0.0709	0.64±1.46	0.83±0.51	0.2427
L-cur (1/cm)	1.09±1.11	0.86±0.71	0.2006	1.07±1.00	0.99±0.66	0.6194
Stress-P_1 (kPa)	94.3±89.2	51.2±55.7	0.0418	8.87±9.39	3.00±2.30	0.0290
Strain-P_1	0.43±0.20	0.51±0.17	0.2603	0.08±0.07	0.07±0.06	0.9860

Data is based on quarter mean values. Values are expressed as mean±standard deviation. Abbreviations as in Table 2.

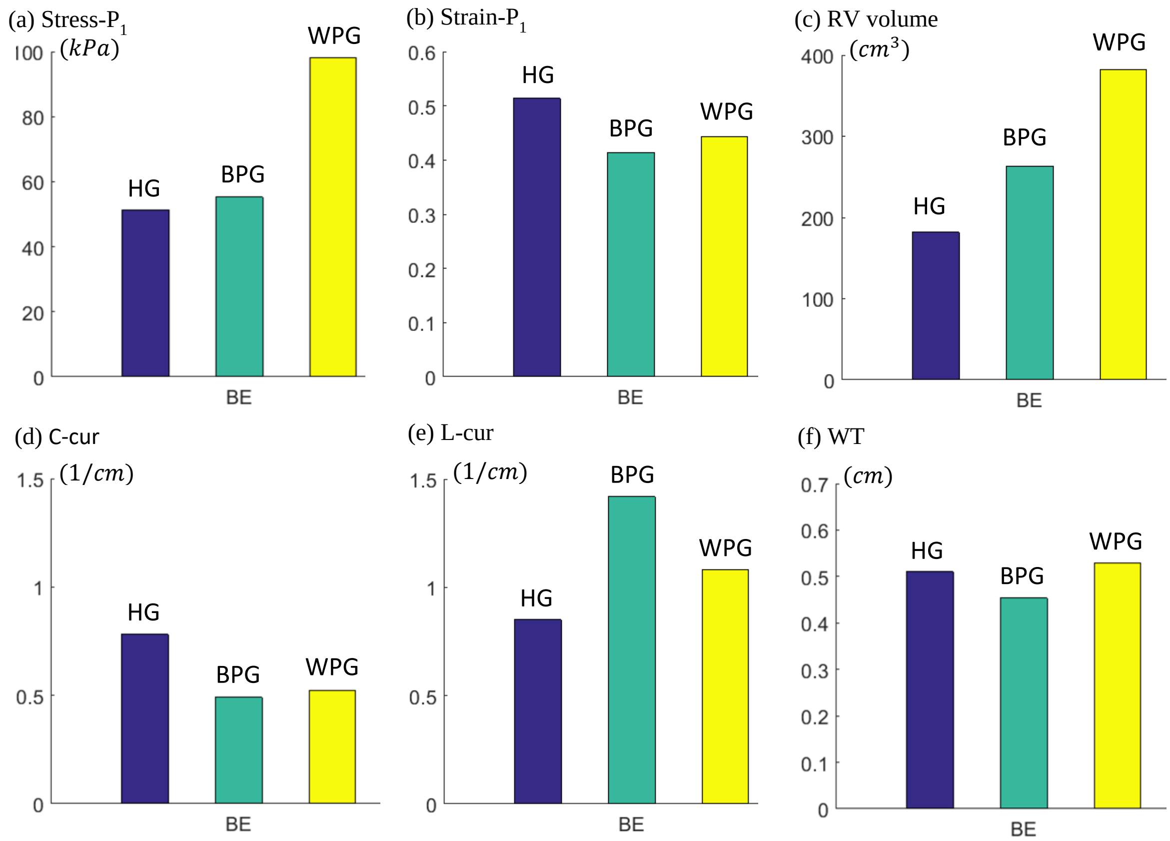

Figure 7. Bar plots comparing average Stress-P$_1$, Strain-P$_1$, RV volume, C-cur, L-cur and WT values from Healthy Group (HG), Better-outcome Patient Group (BPG) and Worse-outcome Patient Group (WPG) at Begin-Ejection (BE). Blue: HG; Green: BPG; Yellow: WPG.

4. Discussion

4.1 Modeling techniques for models based on in vivo data with complex geometry

It should be emphasized that the pre-shrink and mesh generation techniques presented in this paper is of general interest for models based on in vivo geometry and of complex structures. In vivo data of organs such as ventricles and arteries are under pressure and internal stress conditions. Most mechanical models require zero-stress geometry as their starting point for stress/strain calculations. Our pre-shrink pressure presented in this paper is a way to obtain the zero-load ventricle geometry as our model starting geometry. Without the shrinking process, as soon as pressure is added to the ventricle, the ventricle will be inflated and its volume will be greater than its in vivo size. This is a major difference between models based on in vivo data and models based on ex vivo data.

It should also be noted that we are using zero-load ventricle geometry in our models, which is not the same as zero-stress geometry. There should still be residual stress in the zero-load geometry. However, obtaining zero-stress geometry involves cutting-open the ventricle to release the residual stress, and then wrapping it up to obtain the residual stress. Not only the numerical procedure is extremely complex, we also do not have real data about how much the ventricle would open to perform the open-close process. Therefore, it should be understood that zero-load geometry was used as an approximation to the zero-stress geometry.

4.2 Motivation to construct models of healthy people

TOF patients have mixed results after PVR. It has remained challenging for the surgeons and clinicians differentiate patients with better outcome from those with worse outcome. This paper is trying to see if information from healthy people could be helpful in meeting that challenge. At the same time, general mechanical stress/strain and morphological information for healthy people will be good contributions since such data are still lacking in the current literature.

It should be explained that our purpose is not only looking for differences between TOF patients and healthy people. We were also trying to find methods and indicators which could help us to separate BPG from WPG by using HG information. As the main result of this paper, it was found that BPG Stress-P_1 and HG Stress-P_1 were close to each other. In fact, they were not statistically different. This indicates RV stress could be a biomarker to be used for possible prediction of post-PVR outcome. RV volume and longitudinal curvature could serve the same purpose in a similar way.

4.3 Limitations

One limitation of this study is the small sample size which results in limited statistical power. The reason for the small sample size is the extensive amount of the time required for constructing each computational model. Under the current status of computer technology, it takes approximately 1 month to generate one 3D patient-specific model. Thus, improving the model-building technique to make the process less labor-intensive and more clinically applicable will be a major effort of our future work.

Several improvements can be added to our current models for more accurate results: a) fluid-structure interactions can be added to obtain blood flow velocity and shear stress which can be also included in the investigation of predictors for good recovery after PRV; b) patient-specific and location-specific measurements of tissue mechanical properties (such as MRI with tagging) will be very desirable for improved accuracy of our models; c) inclusion of patient-specific fiber orientations; d) inclusion of pulmonary valve mechanics in the current model.

5. Conclusion

Our preliminary results indicated that RV stress from the better-outcome patient group was close to stress from the healthy group and could be used as a potential indicator to differentiate BPG patients from WPG patients, with further validations.

Funding:

This research was supported in part by National Heart, Lung and Blood Institute grants R01 HL089269 (PI del Nido, Tang, Geva), R01 HL63095 (PI del Nido) and 5P50HL074734 (PI: Geva). Tang's research was also supported in part by National Sciences Foundation of China grants 11672001, 81571691.

Conflict of Interest:

The authors declare that they have no conflict of interest.

Ethical approval:

This study was approved by the Boston Children's Hospital Committee on Clinical Investigation. The Boston Children's Hospital IRB approval number is: IRB-CRM09-04-0237.

References

1. McCulloch, A. D., Waldman, L., Rogers, J., Guccione, J. M. (1992) Large-scale finite element analysis of the beating heart. *Critical Reviews in Biomedical Engineering* **20,** 427-449.
2. Hunter, P. J., Pullan, A. J., Smaill, B. H. (2003) Modeling total heart function. *Annual Review of Biomedical Engineering* **5,** 147-177.
3. Pfeiffer, R. E., Tangney, R. J., Omens, H. J., McCulloch, A. D. (2014) Biomechanics of cardiac electromechanical coupling and mechanoelectric feedback, *Journal of Biomechanical Engineering* **136,** 021007.
4. Trayanova, A. N., Rice, J. J. (2011) Cardiac electromechanical models: from cell to organ, *Frontiers in Physiology* **2,** 00043.
5. Nollert, G., Fischlein, T., Bouterwek, S., Bohmer, C., Klinner, W., Reichart, B. (1997) Long-term survival in patients with repair of tetralogy of Fallot: 36-year follow-up of 490 survivors of the first year after surgical repair. *Journal of The American College of Cardiology* **30,** 1374-1383.
6. McKenzie, E. D., Khan, M. S., Dietzman, T. W., Guzm an-Pruneda, F. A., Samayoa, A. X., Liou, A., et al. (2014) Surgical pulmonary valve replacement: a benchmark for outcomes comparisons. *Journal of Thoracic and Cardiovascular Surgery* **148,** 1450-1453.
7. Waien, S. A., Liu, P. P., Ross, B. L., Williams, W. G., Webb, G. D., McLaughlin, P. R. (1992) Serial follow-up of adults with repaired tetralogy of Fallot. *Journal of The American College of Cardiology* **20,** 295-300.
8. Burchill, L. J., Wald, R. M., Harris, L., Colman, J. M., Silversides, C. K. (2011) Pulmonary valve replacement in adults with repaired tetralogy of Fallot. *Journal of Thoracic and Cardiovascular Surgery* **14,** 92-7.
9. Therrien, J., Siu, S. C., McLaughlin, P. R. (2000) Pulmonary valve replacement in adults late after repair of tetralogy of Fallot: are we operating too late? *Journal of The American College of Cardiology* **36,** 1670-1675.
10. Meijboom, F. J., Roos-Hesselink, J. W., McGhie, J. S., Spitaels, S. E., van Domburg, R. T., Utens, L. M., et al. (2008) Consequences of a selective approach toward pulmonary valve replacement in adult patients with tetralogy of Fallot and pulmonary regurgitation. *Journal of Thoracic and Cardiovascular Surgery* **135,** 50-55.
11. Vliegen, H. W., Van Straten, A., De Roos, A., Roest, A. A., Schoof, P. H., Zwinderman, A. H., et al. (2002) Magnetic resonance imaging to assess the hemodynamic effects of pulmonary valve replacement in adults late after repair of tetralogy of Fallot. *Circulation* **106,** 1703-1707.
12. Tweddell, J. S., Simpson, P., Li, S. H., Dunham-Ingle, J., Bartz, P. J., Earing, M. G., et al. (2012) Timing and technique of pulmonary valve replacement in the patient with tetralogy of Fallot. *Journal of Thoracic and Cardiovascular Surgery* **15,** 27-33.
13. Tang, D., Yang, C., Geva, T., del Nido, P. J. (2010) Image-based patient-specific ventricle models with fluid-structure interaction for cardiac function assessment and surgical design optimization. *Progress in Pediatric Cardiology* **30,** 51-62.
14. Tang, D., Yang, C., Geva, T., del Nido, P. J. (2008) Patient-specific MRI-based 3D FSI RV/LV/Patch models for pulmonary valve replacement surgery and patch optimization. *Journal of Biomechanical Engineering* **130,** 041010.
15. Tang, D., Yang, C., Geva, T., Gaudette, G., del Nido, P. J. (2011) Multi-physics MRI-based two-layer fluid-structure interaction anisotropic models of human right and left ventricles with different patch materials: cardiac function assessment and mechanical stress analysis. *Computers & Structures* **89,** 1059-1068.
16. Yang, C., Tang, D., Geva, T., Rathod, R., Yamauchi, H., Gooty, V., et al. (2013) Using contracting band to improve right ventricle ejection fraction for patients with repaired tetralogy of Fallot: a modeling study using patient-specific CMR-based 2-layer anisotropic models of human right and left ventricles. *Journal of Thoracic and Cardiovascular Surgery* **145,** 285-293.
17. Geva, T., Gauvreau, K., Powell, A. J., Cecchin, F., Rhodes, J., Geva, J., et al. (2010) Randomized trial of pulmonary valve replacement with and without right ventricular remodeling surgery. *Circulation* **122(11 Suppl),** S201-208.
18. Tang, D., Yang, C., Geva, T., del Nido, P.J. (2014) Right ventricular local longitudinal curvature as a marker and predictor for pulmonary valve replacement surgery outcome: an initial study based on preoperative and postoperative cardiac magnetic resonance data from patients with repaired tetralogy of Fallot. *Journal of Thoracic and Cardiovascular Surgery* **147,** 537-538.
19. Sanchez-Quintana, D., Anderson, R., Ho, S. Y. (1996) Ventricular myoarchitecture in tetralogy of Fallot. *Heart* **76,** 280–286.
20. Humphrey, J. D. (2002) Cardiovascular Solid Mechanics. *New York: Springer-Verlag*.
21. Tang, D., Yang, C., del Nido, P. J., Zuo, H., Rathod, R. H., Geva, T., etc. (2015) Mechanical stress is associated with right ventricular response to pulmonary valve replacement in patients with repaired tetralogy of Fallot mechanical stress, *Journal of Thoracic and Cardiovascular Surgery* **151,** 687-694.